Multiplexed 3D Analysis of Cell Plasticity and Immune Niches in Melanoma

Clarence Yapp[1,2,*], Ajit J. Nirmal[1,2,3,*], Felix Zhou[4], Zoltan Maliga[1], Paula Montero Llopis[5], George F Murphy[6], Christine G Lian[6], Gaudenz Danuser[4], Sandro Santagata[1,2,6,7] and Peter K. Sorger[1,2,7,†]

[1]Laboratory of Systems Pharmacology, Department of Systems Biology, Harvard Medical School, Boston, MA, 02115, USA.

[2]Ludwig Center at Harvard, Harvard Medical School, Boston, MA, 02115, USA.

[3]Department of Dermatology, Brigham and Women's Hospital, Harvard Medical School, Boston, MA, 02115, USA.

[4]Lyda Hill Department of Bioinformatics, UT Southwestern Medical Center, Dallas, TX, 75390, USA.

[5]Microscopy Resources on the North Quad (MicRoN), Harvard Medical School, Boston, MA 02115, USA.

[6]Department of Pathology, Brigham and Women's Hospital, Harvard Medical School, Boston, MA, 02115, USA.

[7]Department of Systems Biology, Harvard Medical School, 200 Longwood Avenue, Boston, MA 02115, USA.

*Authors contributed equally

†Corresponding Author; peter_sorger@hms.harvard.edu

ORCID:

Clarence Yapp - 0000-0003-1144-5710

Ajit J. Nirmal - 0000-0003-4139-0618

Felix Zhou- 0000-0003-4463-1165

Zoltan Maliga- 0000-0003-4209-7253

Paula Montero Llopis- 0000-0002-5983-2296

George Murphy- 0000-0001-9362-5146

Christine Lian- 0000-0003-4626-1612

Gaudenz Danuser- 0000-0001-8583-2014

Sandro Santagata - 0000-0002-7528-9668

Peter K Sorger - 0000-0002-3364-1838

SUMMARY

Homeostasis of normal tissues and the emergence of diseases such as cancer are controlled by changes in the proportions and states of diverse cell types, cell-cell interactions, and acellular components of the tissue microenvironment[1]. Spatial omics using highly multiplexed tissue profiling[2] makes it possible to study these processes *in situ*, usually on thin, 4-5 micron thick sections (the standard histopathology format)[3]. Microscopy-based tissue imaging is commonly performed at a resolution sufficient to determine cell types but not detect the subtle morphological features associated with cytoskeletal reorganisation, juxtracrine signalling, or membrane trafficking[4]. Here we introduce a 3D imaging approach using existing instruments and reagents that is able to characterize a wide variety of organelles and structures at sub-micron scale while simultaneously quantifying millimetre-scale spatial features. We perform high-resolution 54-plex cyclic immunofluorescence (CyCIF) imaging[3] on sections of primary human melanoma thick enough (30-40 microns) to fully encompass two or more layers of intact cells. In pre-invasive melanoma *in situ*[5], 3D imaging of entire cell volumes showed that transformed melanocytic cells are plastic in state and participate in tightly localised niches of interferon signalling near sites of initial invasion into the underlying dermis. Below this layer, immune cells engaged in an unexpectedly diverse array of membrane-membrane interactions as well as looser "neighbourhood" associations[6]. These data provide new insight into the transitions occurring during early tumour formation and demonstrate the potential for phenotyping tissues at a level of detail previously restricted to cultured cells and organoids.

MAIN

Tissue specimens from human patients are complex in composition and organization, and spatial profiling overcomes this by collecting highly multiplexed data. In spatial transcriptomics[7], the ability to discriminate cell types and states depends primarily on the number of genes assayed. In high-plex tissue imaging, both the number of antigens and their morphologies yield important information. However, tissue specimens can be large (up to 10^7 cells) so image resolution is commonly sacrificed in favour of throughput using relatively low scanner magnifications (0.6 to 2.0 µm pixel sizes); as a result, intracellular structures and subtle changes in cell shape cannot easily be quantified. We therefore modified CyCIF for high resolution 3D imaging using commercial antibodies and a widely available Zeiss LSM980 multi-spectral confocal microscope. Panels of up to 52 antibodies were developed to discriminate among cell types, assay inflammatory and immunoregulatory processes and visualize tissue architecture. Type I and II collagen were visualized on the same section using Second Harmonic Generation (SHG) by Fluorescence Lifetime Imaging Microscopy (see **Methods**). We balanced resolution, axial sectioning depth, antibody penetration, etc. (**Supplementary Methods**) in a 3D CyCIF protocol for specimens with a thickness

of ~35 µm at voxel dimensions of 140 nm x 140 nm x 280 nm (200 to 500 voxels per cell**; Fig. 1a**) while keeping data size below ~500 gigabyte per mm^2 of tissue

To study how specimen thickness impacted assessment of cell type and morphology, FFPE blocks were sectioned at multiple thicknesses ranging from 5 to 40 µm (sections thicker than 40 µm were difficult to handle and will require new processing techniques). Following sectioning, standard dewaxing and antigen retrieval procedures were used, followed by multi-cycle 3D CyCIF. We found that, in conventional 5 µm thick sections, nearly all nuclei (>90%) were incomplete along the Z axis. However, in 30-40 µm sections, 60-80% of nuclei had complete nuclear envelopes along all three axes (**Fig. 1b,c; Supplementary Video 1**). In many areas of the specimen, multiple layers of intact nuclei were visible. Because high resolution 3D data are hard to reduce to 2D images, images in this paper comprise either single image planes or volumetric reconstructions generated using Imaris® software (RRID:SCR_007370); all primary data are available for download and review using the free Imaris Viewer.

We then captured 3D images of two serial 35 µm thick tissue of a stage 2c primary cutaneous melanoma[8] (**Supplementary Table 1**) obtained from the pathology archives of the Brigham and Women's Hospital. This specimen involves a *melanoma in situ* (MIS) with some features of an earlier precursor stage adjacent to an invasive vertical growth phase melanoma (**Supplementary Fig. 1**). The primary section was analysed using 52 antibodies, Hoechst 33342 for DNA, and SHG for collagen (Dataset 1; **Fig. 1d & e; Supplementary Fig. 2**; **Supplementary Table 2**) and an adjacent section was imaged with 41 antibodies and Hoechst 33342 for DNA (Dataset 2; **Supplementary Table 3**). Data from additional 5 µm sections of the same specimen were used to confirm antibody specificity and performance (see **Methods**). Using a newly developed 3D segmentation algorithm and UMAP embeddings we could distinguish major immune and tumour cell states (**Fig. 1f**). The MIS and underlying dermis in our specimen were not highly proliferative, with only 1% of cells (n = 110) positive for the $Ki67^+$ proliferation marker (proliferation is known to vary widely among MIS specimens)[9]. Among the $Ki67^+$ cells, 34% were T cells while the remainder consisted of monocytes (28%), and few endothelial cells (2.7%) (markers used to assign cell types are described in **Supplementary Fig. 3**). Only a single melanocytic cell was $Ki67^+$. By contrast, 11% of all types of cells in the invasive tumour domain were proliferative. Tumour cells were the most abundant $Ki67^+$ cells (45%), consistent with their oncogenic transformation, followed by monocytes (44%). The fraction of proliferating T cells was 21-fold greater in the invasive domain than in MIS, implying a higher level of immune cell activation.

Immune cells in the dermis are known to associate with collagen fibres,[10–13] and in the MIS, this was most evident for B cells (**Fig. 1g;** collagen was largely absent from the invasive tumour). B cells were often (n = 11 of 14 in the MIS) stretched into irregular shapes, distinct from the round morphology observed for B cells in blood (visualized as 2D section and 3D rendering in **Fig. 1h & i**). Complex multi-cellular structures were also discernible, such as a 100 µm-long dermal blood vessel

(**Fig. 1j; Supplementary Video 2)**, in which ~10 vimentin and beta-catenin-containing endothelial cells formed a tube enclosing erythrocytes and a neutrophil. At the distal end, a T-helper cell and myeloid cell were visible where the vessel appeared to branch. Most remarkable was a B cell with a sphericity value of ~0.35 that was flattened against the vessel wall, a morphology consistent with diapedesis, a process whereby immune cells exit blood vessels and infiltrate tissues[14]. These features were not evident in virtual 5 µm-thick sections (**Supplementary Fig. 4**). Elsewhere in the dermis, another B cell had its nucleus traversing a vessel wall while its cell body remained inside the vessel (**Supplementary Fig. 5**). Only recently have functions been ascribed to B cells in the skin, and our images provide direct evidence of B cell recruitment from the vasculature into the dermis, at densities consistent with recent findings[15].

Intracellular features and cell packing

We found that it was possible to resolve and quantify a variety of membranous and punctate structures in both immune and tumour cells, including peroxisomes (based on catalase staining in dendritic cells; **Fig 2a**), secretory granules and/or ER (lysozyme C in neutrophils and granzyme B in T cells; **Fig 2a-b**), cell surface receptors (PD1 and LAG3 immune checkpoint proteins; **Fig. 2b**), DNA damage foci (γH2AX in neutrophils; **Fig. 2c**), mitochondria (COX IV), and biomolecular condensates (MX1 in CD4 T cells; **Fig. 2d**). Lineage-associated differences in the shapes of the nuclear lamina could also be determined, for example, the tri-lobed nucleus of neutrophils (**Fig. 2e**), as well as structures associated with cell polarity, such as microtubule organising centres (**Fig. 2f**)**.** Simultaneous staining for multiple lineage markers made it possible to identify the types of cells in which each structure was found (e.g., keratinocytes and myeloid cells for γH2AX foci and dendritic cells for catalase foci). These data enable detailed analysis of intracellular organelles and nuclear condensates in the context of native tissue (**Fig. 2g)** and also make it possible to precisely phenotype cells (see below)[16].

Across the specimen, cells were densely packed except in areas in which vessels or ECM filled the voids (**Fig 2h; Supplementary Video 3**). Intact nuclei averaged 5.0 µm in diameter (mean 7.2 µm ± 2.3 µm SD for melanocytes and 4.9 µm ± 2.8 µm for immune cells). Cells averaged 13 µm ± 4.3 µm along the major axis and 6.1 µm ± 1.9 µm along the minor axis (consistent with recent and historical estimates),[17] emphasising that cytoplasms (scored as distance from the plasma membrane to the nuclear lamina) are only 1 to 6 µm thick (**Fig 2i-j)**. Cells such as melanocytes and Langerhans cells had highly extended processes that spanned several nuclear diameters, although transformed melanocytic cells were more rounded (see below). Tight cell packing, extended processes, and inevitable overlap along the Z-axis explains why accurate single-cell segmentation, for example in 2D microscopy images and spatial transcriptomics[18], is challenging**.** We also found that 3D analysis was essential for accurately capturing cell shape. For example, viewing the invasive tumour from 2D images suggested that round cells were more common in the tumour centre and elongated cells at the tumour margin. However, in 3D we saw that this difference was an artefact of differences in

orientation: cells in the centre were more likely to be viewed end-on whereas those in the margin were rotated ~90° (**Fig 2k-m).**

Cell shape and the forces that cells exert to move, are regulated by the actomyosin cytoskeleton. In both MIS and invasive tumour, dendritic cells and T cells had the most prominent actin cytoskeletons (~2-fold more actin overall than melanocytic cells and 3-fold more than in keratinocytes; **Supplementary Fig. 6**). This comprised a dense network of plasma membrane-proximal cortical actin, consistent with the migratory properties of these cells (**Fig. 2n-o**). Tumour cells had the least distinct actin networks, with little evidence of stress fibres or similar structures. Instead, actin was often found in plasma membrane-localised puncta, particularly in the interior of the invasive tumour (0.45 puncta per cell in the interior vs. 0.06 per cell at the tumour margin**; Fig. 2p-q; Supplementary Fig. 6**), that may represent invadopodia[19]. Phosphorylation of myosin light chains helps regulate tension and actomyosin contractility, which play in key role in cell motility. We found that tumour cells at the margin of the invasive domain (dotted line **Fig. 2p**) but not in the interior were pMLC2 positive, as were most myeloid cells, consistent with the notion that tumour cells at the invasive front acquire an amoeboid phenotype with elevated contractility[20]. In the MIS, however, pMLC2 was most commonly expressed on neutrophils. Theoretical and experimental studies on cell migration have demonstrated a dependency not only on the intrinsic properties of cells and their cytoskeletons but also on cell shape and packing[21]. We speculate that accurate 3D representations of tumours and their cytoskeletons will become important in such studies.

Variability in melanocyte states and neighbourhoods

The molecular events that initiate melanoma formation are not fully understood[22] and the presence of melanoma precursor fields[5] and MIS is scored based on changes in the morphologies, numbers, and positions of melanocytic cells, most commonly in H&E images[23]. 3D images of MIS demonstrated the presence of cells exhibiting the highly dendritic morphology of normal melanocytes and wrapping around neighbouring keratinocytes (an arrangement that promotes transfer of UV-protective melanin; **Fig. 3a**). Also present were pagetoid melanocytic cells that lacked dendrites and had a rounded, ameboid morphology (cytological atypia), which was most obvious among cells that had migrated upwards into the epidermis (**Fig. 3b-h)**. This type of pagetoid spread involved single cells as well as small groups of cells and is a hallmark of oncogenic transformation[24].

The genetic mutations associated with later stage melanoma are well understood[25], but mechanisms of malignant transformation during melanoma initiation remain elusive. A handful of studies have identified oncogenic mutations (such as BRAF, NRAS, NF1)[25] and reductions in the DNA epigenetic marker, 5-Hydroxymethylcytosine (5hmc)[26] in melanoma precursors. This suggests that both genetic and epigenetic changes play a pivotal role in cancer onset. Given the historical difficulty of studying the early precursor phase, with its small specimens and few melanocytic cells, the majority of research on melanoma progression markers (e.g. PRAME[27,28]) has been performed

in advanced, invasive melanoma. However, 3D CyCIF provides a sensitive means of studying melanoma initiation at a single cell level.

We scored individual cells for expression of six markers of melanocyte lineage and transformation in melanocytic cells (n=875) of the MIS, including 5hmc, PRAME, MART1 (a melanocyte cell surface protein used to detect melanoma), SOX9, SOX10, and MITF (transcription factors associated with differentiation). The six markers were present in all 63 possible combinations, without evidence of significant spatial correlation (**Fig. 3 i-s**). Cells undergoing pagetoid spread were also observed to express many different combinations of lineage markers (**Fig 3c-h**). Particularly striking were all possible combinations of transcription factors such as SOX9 and SOX10 (**Fig. 3 m,n**), which are associated with neural crest cells (de-differentiated lineages) and MITF (a key regulator of melanocyte differentiation). In the case of SOX9 and SOX10, there was also clear evidence of a graded transition between states (**Fig. 3t**). However, we did not detect expression of the neural crest marker NGFR (CD271) in any cell in the MIS or invasive tumour (as a control, we confirmed positive staining for NGFR in parallel thin-section studies with metastatic melanomas); NGFR positivity has been proposed to be a marker of melanoma initiating "stem" cells[29]. Moreover, we did not detect any association between cell-intrinsic markers and melanocyte morphology or other distinctive features, such as the nuclear actin rods that were found in ~14% of melanocytic cells in MIS but not elsewhere in the specimen (**Fig 3q-r**; **Supplementary Figure 7)**. The presence of these rods has been associated with a stress response[30] and may reflect contact between rod-positive cells and one or two activated $CD8^+$ $PD\text{-}1^+$ cytotoxic T cells (<1.5 μm membrane-to-membrane distance – **Fig 3q**). These data imply that melanocytic cells with features of early malignant transformation are subject to frequent changes in cell state (phenotypic plasticity) rather than progressive evolution from a single transformed or progenitor (stem-like) cell, as observed in advanced invasive melanoma.

We also observed changes in immunogenic state affecting clusters of cells (cellular neighbourhoods), consistent with cell non-autonomous regulation. For example, the MIS contained three spatially restricted domains in which the levels or distributions of IRF1, MX1, and MHC-I revealed an active response to interferons (IFNs; **Fig 4a-b)**[31]. IRF1 is an IFN-responsive transcription factor that translocates from the cytoplasm to the nucleus and MX1 and MHC-I are two downstream response genes; MX1 forms distinctive biomolecular condensates[32] and MHC-I is found on the cell surface. The ~ 50 to 100 μm extent of the inferred IFN-positive domains implies highly localised cytokine activity (the size of the domains was confirmed on a distant serial section; **Supplementary Fig. 8, 9**). Within these domains, melanocytic cells had started to pass through the DEJ and were in contact with immune cells (**Fig 4 b-c)**. Thus, our data provide direct evidence for restricted and recurrent spatial niches, defined by the simultaneous presence of an IFN response, melanocyte-immune cell contact, and melanocytes crossing the DEJ (the first step in invasion). These IFN-positive spatial niches were coincident with the phenotypic switching described above

but without delectable spatial correlation, despite evidence that IFN can induce melanoma de-differentiation in tumours and cultured melanoma cells[33].

Memory T cell subsets

In domains characterized by IFN-positivity, along and just below the DEJ, we observed an enrichment of dendritic cells, intermingled with $CD4^+$ and $CD8^+$ T cells. The normal epidermis is known for its abundance of $CD103^+$ resident memory T cells, which are derived from prior encounters with non-tumour antigens[34]. This makes it challenging to distinguish T cells recruited from the circulation from those already residing in the skin. We expect tumour reactive T cells along the border of the invasive tumour domain, where $CD8^+$ T cells co-expressed PD-1 and/or LAG3, consistent with terminal exhaustion. Very few tumour cells expressed detectable PD-L1 in either the MIS or invasive tumour region and juxtacrine interactions with $CD8^+$ $PD\text{-}1^+$ T cells involved PD-L1-expressing dendritic cells almost exclusively, consistent with previous data showing that myeloid cells are the primary source of immunosuppressive PD-L1 in early-stage melanoma[8].

Across the MIS, invasive tumour, and underlying dermis we identified $CD3^+$ T cells that were positive or negative for CD4, CD8, CD103, PD-1, LAG3, GZMB, and Ki67 in every possible combination (some CD4 positive cells were also $CD3^-$). Among CD8 T cells (n=9940), the greatest proportion (89%) were positive for CD103 and of these, most were positive for $PD1^+$ and/or $LAG3^+$ (markers of exhaustion; **Fig, 4d-i**). In contrast, exhausted $CD8^+$ $CD103^-$ states were less common, with 5.3% $PD1^+$ and/or $LAG3^+$. Of particular interest were the CD8 memory T cells with features of exhaustion and cytotoxic activity ("T_{MEA}" cells), as evidence by positivity for the proliferation marker Ki67 and/or Granzyme B (GZMB; a protease released by cytotoxic lymphocytes to kill infected or transformed cells; **Fig. 4e,g,h**). Roughly half of these T_{MEA} cells were in proximity to melanocytic cells (based on scoring the five nearest neighbours; **Fig. 4d,j**, yellow box). Recent studies have identified a distinct set of "progenitor of exhaustion" memory T cells (T_{PEX} cells)[35–37] that express exhaustion and memory markers, and can be re-activated by immune checkpoint inhibitors[38]. A key feature of T_{PEX} cells is expression of the TCF1 master regulatory transcription factor; unfortunately, TCF1 staining was available only in dataset 2, which had fewer T cell markers. In this dataset less than 0.5% of $CD8^+$ $PD\text{-}1^+/LAG3^+$ cells were TCF1 positive and thus bona fide T_{PEX} cells (**Supplementary Fig 10**). We conclude that T_{MEA} cells are distinct from T_{PEX} cells, and that both lineages represent T cell states with relatively long-lived or re-activatable cytotoxic activity.

We also observed a diversity of CD4 T cells (n=2181); ~40% were T_{REG} cells and ~60% were T_{helper} cells (**Fig 4k**). Among the helper cells, 7% had features of activation (Ki67 and/or GZMB positivity) and about half of these also expressed PD1. CD103 is not expressed in any CD4 cells, but we observed a distinct pattern of GZMB staining: diffuse globular staining in CD4 T cells as opposed to punctate staining in CD8 T cells consistent with cytoplasmic granules. Globular GZMB has previously been described as a feature of activated memory $CD4^+$ T cells[39] that are effective at tumour control.[40]. We propose that these represent CD4 T_{MEA} lineages.

Immune niches on varying spatial scales

Spatial statistics is commonly applied to tissue images to quantify how cells are organised into local and regional communities[8]. When we analysed 2D projections of 3D data using spatial latent dirichlet allocation (LDA) to identify recurrent cellular neighbourhoods (RCNs) (**Supplementary Fig. 11**), we captured the overall organisation of immune cells in the MIS and invasive tumour. However, visual review of the RCNs revealed another level of cellular organisation based on the type of membrane-membrane interaction: (i) direct binding (Type I) (ii) membrane apposition (Type II) and (iii) neighbourhood clustering (Type III). Direct binding was characterised by overlapping membranes from neighbouring cells. This was most obvious in the case of a $CD8^+$ $PD1^+$ T cell interacting with a rare PD-L1 expressing melanocytic cell (**Fig. 5a**). A line integral across the cell-cell junction (followed by polynomial curve fitting) revealed a membrane-to-membrane spacing of ~70 nm (**Fig. 5b**). This contrasted with an average intermembrane spacing across the specimen of ~1.5 µm. PDL1 expressing dendritic cells bound to $CD8^+$ $PD1^+$ T cells had a similar membrane spacing (**Fig. 5c,d**). In some cases, it was possible to discern multiple foci of PD1 PDL1 interaction in the contacting membrane area (tens of square microns; 13 foci in **Fig. 5e-g**). Another Type I interaction involved a $CD8^+$ $PDL1^+$ $LAG3^+$ $GZMB^+$ $Ki67^+$ T_{MAE} cell and a melanocytic cell in the MIS cell with an intermembrane distance of ~60 nm (**Fig. 5h-j**). Given the resolution of our microscope, this spacing seems consistent with EM of immunological synapses showing integrin-stabilised cell-cell contacts and intervening clefts with ~30 nm membrane separation[41].

A second form of cell-cell interaction involved neighbouring cells with extensive membrane apposition without evidence of direct overlap; in this case membrane-membrane spacing of 300-600 nm was typical (**Fig 5k,l**). This gave rise to recurrent assemblies such as the two $CD4^+$ $FOXP3^-$ $MX1^+$ T cells bound to three exhausted $CD8^+$ $LAG3^+$ $CD103^-$ T cells (**Fig 5m,n; Supplementary Video 4)**. Type II CD4 CD8 interactions were common across the MIS, without evidence of a nearby antigen presenting cell (e.g., dendritic cell), making this an atypical interaction with respect to the current understanding of T cell biology. In the conventional mode, APCs present antigens to both CD4 and CD8 T cells, with the CD4 helper cells enhancing the cytotoxicity of CD8 cells via cytokine production.

A third form of cell-cell interaction involved an intermembrane spacing of ~500 nm but only along a small area of the membrane (1-2 μm^2); such interactions could involve 100 or more immune cells, a pattern we have described previously as lymphocyte networks (lymphonets)[6]. We observed lymphonets comprised primarily of CD4 T cells or CD8 T cells (**Fig. 5o**), dendritic cells (**Fig. 5p)** and mixtures thereof. Lymphonets did not contain $CD4^+$ $FOXP3^+$ regulatory T cells, which were most commonly involved in Type 1 interactions (**Fig. 5q**), or tissue-resident macrophages, which were nearly uniformly distributed across the dermis. Lymphonet formation is thought to be mediated by local release of chemokines, and we found that many networks contained one or more MX1 positive cells. A distinct form of cell-cell interaction was observed among B cells in the region of invasive

tumour: hundreds of B, T and dendritic cells formed assemblies resembling nascent tertiary lymphoid structures (TLS) but lacking fully formed germinal centres (**Fig. 5r; Supplementary Fig. 12**). TLS play an important role in the responsiveness of metastatic melanoma to immunotherapy[42] and have been detected previously in some primary melanomas[43]; lymphonets with the properties of immature TLS have also been observed in murine tumors[6].

The three types of interactions described above often co-occurred. **Fig. 6a,b** shows a complex set of cell-cell interactions involving a melanocytic cell at the DEJ (cell 1) and 10 immune cells (cells 2-11; **Fig. 6c, Supplementary Video 5**). In this network, a $CD4^+$ $GZMB^+$ memory T_{MAE} cell (cell 2) forms a Type I contact with a $CD8^+$ $LAG3^+$ $CD103^+$ $PD1^-$ memory T cell (cell 3; **Fig. 6d**) with an estimated membrane-membrane spacing of 30 nm over a 20-30 um^2 area (**Fig. 6e)**. Cell 3 makes an extended Type II contact with another memory $CD8^+$ $CD103^+$ $LAG3^+$ $PD1^-$ T cell (cell 5; 150 nm spacing **Fig. 6f**). Cell 4 and 5 make an interaction (640 nm spacing) that we score as a Type III because it is spatially restricted (**Supplemental Figure 13**). CD4 T cell 2 also engages in Type II contact with a melanocytic cell (1; 690 nm spacing; **Fig. 6g,h**). The two cells are proximate over a much larger area, but we judge the 1.1 µm spacing to be a consequence of packing rather than interaction (**Fig. 6i**). Elsewhere in the network, Type I interactions were observed between CD4 T cell 5 and a dendritic cell (cell 6) and cell 6 and a CD4 T_{REG} cell (cell 8); finally, a $CD8^+$ network (cells 9-11) extended in an epidermal direction (**Fig 6c**). Complex networks such as this were evident throughout the tissue but required visual review, making precise quantification difficult. Nonetheless, the presence of networks of many cell types and states reveals the diversity of positive and negative signals experienced by T cells within a highly restricted spatial domain.

Conclusions

Our data reveal striking features of tumour and immune compartments in an early-stage melanoma. At the precursor-MIS stage, these tumours are not yet highly mitotic but are starting to invade the dermis and undergo pagetoid spread into the hostile environment of the epidermis. We find that these cells access every possible combination of the six lineage and epigenetic markers assayed, implying a high degree of plasticity. Plasticity is well described in late-stage melanoma and cell lines[44], but our data suggest it is also a feature of early stage disease. One state missing from this specimen and other early melanomas studied by CyCIF[8], is an NGFR-high state, which has been described as a neural crest (stem-like) tumour-initiating state. Although $NGFR^+$ cells are common in later stage melanoma, our data suggest that they arise after an invasive cancer has formed. Overlaying this cell type plasticity (but not obviously correlated with it) are spatially restricted inflammatory domains – often only a few cell diameters wide. Spatially restricted cytokine signalling is predicted by mathematical models of cytokine production and uptake under conditions of high consumption[45].

Our data demonstrate the possibility of studying, in preserved human tissues, phenotypes and intracellular structures that have hitherto been examined primarily in cultured cells; this includes the numbers and morphologies of organelles, condensates, and receptor complexes. We find that 3D imaging of tissues containing at least one full cell layer is essential: many subcellular organelles cannot be unambiguously assigned to a cell in thin sections. Precise 3D phenotyping has revealed high diversity in expression of T cell lineage markers such as CD3, CD4, CD8, CD103, PD1, PDL1, and LAG3 checkpoint proteins, and GZMB, MX1, and Ki67 state markers. Skin is rich in $CD8^+$ $CD103^+$ memory cells and we find that a substantial fraction of these express markers of exhaustion and activation, potentially making them analogous to the T_{PEX} cells thought to be a primary target of immune checkpoint inhibitors[35–37].

The use of spatial statistics to analyse high-plex tissue images[46,47] is currently based on nuclear position to score proximity and identify cell-cell interactions. However, analysis of membrane contacts provides a different perspective and suggests three classes of cell-cell interaction: (i) direct binding, in some cases attributable to PD1-PDL1 interaction (with a spacing estimated, by polynomial curve fits to intensity profiles, of as little 30 nm) (ii) membrane apposition involving extended membrane areas (~20 μm^2) but greater membrane-membrane spacing (~300-600 nm), and (iii) loose cell networks with statistically significant association, some contact, and evidence of IFN signalling but less apposition and looser organisation (lymphonets[6]). Particularly striking was a high frequency of direct (Type I) interaction between CD4 and CD8 T cells without visible involvement of professional antigen presenting cells. The distinctions among these classes are not always unambiguous and, given the dynamic nature of juxtracrine interactions, different types of interaction may represent different points in the time of evolution of a common structure. Regardless, our data show that immune cells can form very complex simultaneous associations with cells of different type including those known to send both positive and negative signals to cytotoxic T cells.

A technical limitation of the current study is that we have collected only two 3D datasets from a single specimen, largely due to a requirement for laborious visual review: a key goal for future work is automated detection and quantification of intracellular features and cell-cell contacts. A specific issue with the MIS described here is that it is proximate to an invasive Grade 2c melanoma that likely drains into the same lymph node; this likely affects the immune environment. A more fundamental limitation is that tissue profiling provides data on a single point in time and many features observable in high-plex, high-resolution 3D data do not have functional correlates. This can be addressed by 3D imaging of co-cultures, organoids, and mouse models subjected to mechanistic and perturbational studies allowing a mechanistic bridge to be built to human tissues. Data-driven reconstruction of individual cells and their organelles in tissue is a near-term prospect, for example, using methods developed by Viana *et al* for 3D reconstruction of cells grown in culture[16].

Acknowledgements

We thank Dr. Tom Kupper, Dr. David Liu, and Dr. Judith Agudo for their feedback on the manuscript and assistance in data interpretation. We thank Alyce Chen, Sabrina Chan, Jeremy Muhlich, and John Hoffer for help in all stages of this project, Juliann Tefft for helpful edits to the manuscript, John Lian for providing annotations for segmentation model training, and Jackson Appelt for performing tissue integrity experiments. We thank the MicRoN core facility at Harvard Medical School for their training and support in the different instruments. We are grateful to Geoff Guimaraes, Tanay Desai, and Samantha Fore from Carl Zeiss for providing a complete LSM980 Airyscan 2 on long-term demo.

Funding

This work was supported by Ludwig Cancer Research and the Ludwig Center at Harvard (P.K.S., S.S.) and by NCI grants U2C-CA233280 and U2C-CA233262 (P.K.S., S.S.), R00CA256497 (A.J.N.), Research Specialist Award R50-CA252138 (Z.M.) and CCBIR grant U54-CA268072 (G.D.). Development of computational methods and image processing software is supported by a Team Science Grant from the Gray Foundation (P.K.S., S.S.), the Gates Foundation grant INV-027106 (P.K.S.), the David Liposarcoma Research Initiative (P.K.S., S.S.), and the Emerson Collective (P.K.S.). S.S. is supported by the BWH President's Scholars Award. Histopathology was supported by P30-CA06516.

Author Contributions

CY, PKS, and AJN developed the concept for the study. CY, ZM and PML collected image data. FZ and GD developed software and performed data analysis in collaboration with CY and AJN. SS GFM and CGL provided specimens and pathology expertise. All authors wrote and edited the manuscript. GD, GFM, CGL, SS and PKS provided supervision.

Competing Interests

PKS is a co-founder and member of the BOD of Glencoe Software, member of the BOD for Applied Biomath, and member of the SAB for RareCyte, NanoString, and Montai Health; he holds equity in Glencoe, Applied Biomath, and RareCyte. PKS consults for Merck and the Sorger lab has received research funding from Novartis and Merck in the past five years. The other authors declare no outside interests.

Materials & Correspondence

All materials associated with this study are available through commercial vendors. Please contact Peter Sorger (peter_sorger@hms.harvard.edu) with any additional requests.

Data Availability (At time of final publication)

All images and derived data (~3 TB) are available without restriction via the NCI Human Tumor Atlas Network Portal (data.humantumoratlas.org/). The Human Tumor Atlas Network participant (specimen) ID numbers are listed in **Supplementary Table 1**. All other data supporting the findings of this study are available via an index page on GitHub that has been archived on Zenodo (doi.org/10.5281/zenodo.10055593). To browse a 2D maximum projection of a subset of this data in Minerva (no download required), please go to www.tissue-atlas.org/mel-3d-mis-2.

Code Availability

Original code associated with this paper is available on GitHub (github.com/labsyspharm/mel-3d-mis) and Zenodo (doi.org/10.5281/zenodo.10055593).

Supplementary Discussion

3D imaging challenges the ability to balance between acquisition time, sensitivity, and most notably, reduction of out-of-focus signal that would otherwise reduce contrast. The latter is required for resolving structures in thick tissue along the axial direction, where the axial resolution depends on wavelength, numerical aperture of the objective lens, axial sampling step size, and pinhole diameter in the case of a confocal. Traditional widefield microscopy can be supplemented with deconvolution to reassign out-of-focus signal back to the focal plane, which requires knowledge of the point spread function and is generally suitable for thin samples[48]. Total internal reflection fluorescence (TIRF) microscopy[49,50] can produce high contrast very thin 3D images when used in conjunction with other techniques such as DNA paint, but is limited to only 100 nm beyond the coverslip and is not suitable for highly multiplexed imaging protocols where the tissue is not mounted to the coverslip. More commonly found in research settings are spinning disk[51] and laser scanning confocal[52,53] microscopes where the latter is much slower due to the need to laser raster but provides finer control over the pinhole diameter, and thus, the size of the optical sectioning and the gain in contrast by rejection of out of focus light. Confocal microscopes are notoriously known for being light inefficient ; between a widefield and laser scanning confocal, orders of magnitude far fewer photons from the sample are rejected and never reach the detector[54] although newer micro lenses and sensitive detectors are able to recapture much of this signal. Additionally, sample thickness at any given point is fully illuminated regardless of which focal plane is currently being imaged and this significantly contributes to photobleaching and challenges in downstream quantitative measurements. In specialized research settings, two-photon excitation (TPE) microscopy[55] uses pulsed mode-locked lasers to excite a femto-litre sized volume via the simultaneous absorption of two photons (typically in the near-infrared range). Two-photon lasers can also capitalize on certain collagen types that emit a label-free second harmonic signal[56–58]; the resulting signal has a wavelength that is precisely half of the incident laser wavelength. Since near-infrared wavelengths

experience less attenuation and contribute to less phototoxicity, TPE is preferred in tissue and intravital imaging. Furthermore, multiple fluorophores can share similar two-photon excitation spectra, therefore, this creates a throughput advantage in thick specimens. However, these systems are less common than confocal microscopes because they are significantly costlier and require specialist knowledge to operate and maintain.

A computationally-intensive solution to combine high-plex imaging with coarse 3D data has been to register several thin serial sections,[59–62] however, the axial resolution of the final dataset is on the order of 5-20 microns and, thus, consists of incomplete cell volumes. A variety of Light Sheet Fluorescence Microscopy (LSFM) and tissue clearing methods[63–65] have been developed to image tissue sections as thick as several mm, with the most recent capable of subcellular resolution, but not all clearing methods are compatible with FFPE tissue[66] and the total number of fluorophores that has been imaged is up to 5 or fewer depending on the optics[67,68]. While spectral unmixing, spillover compensation, or the use of Raman dyes can increase this number to 8-10 channels[69–71], to date, sequential staining and high-plex high-resolution (sub-micrometer scale) imaging of thick sections has not been demonstrated. Efforts are underway to create specialized multiplexed deep imaging microscopes, but we sought to exploit the types of instruments already available in many research institutions so that the detailed cell biology of tissues and tumours might be explored without delay.

Methods

Specimen collection

Specimens were retrieved from the archives of the Department of Pathology at Brigham and Women's Hospital and collected under Institutional Review Board approval (FWA00007071, Protocol IRB18-1363) under a waiver of consent. Two 35 µm serial sections of melanoma (referred to as Dataset 1 and Dataset 2) were used for all experiments. Quantifications are based on Dataset 1. See **Supplemental Table 1** for clinical metadata regarding this specimen and the related HTAN identifiers. The histopathological regions of interest for each specimen were annotated from a serial section consistent with the work of Nirmal, Vallius, Maliga et al. (2022)[8] by a board-certified pathologist based on melanoma diagnostic criteria.

Cyclic immunofluorescence (CyCIF)

A staining plan containing a list of antibodies used can be found in **Supplementary Table 2 and 3**. Antigen retrieval, staining, and bleaching was performed as described in Nirmal, Vallius, Maliga et al. (2022)[8]. Due to the fragile nature of thicker samples, extra care was taken during washes, bleaching and decoverslipping. Antibodies for each cycle were diluted in 400 µl of blocking buffer and stained for 8-10 hours to allow for same-day imaging and at room temperature to encourage penetration of antibodies (see below).

Optimization of sample thickness and antibody staining protocol

We sought to determine an ideal tissue thickness for CyCIF imaging using well-characterized tonsil sections. Based on the maximum working distance of most water and oil-immersion lenses (~200 µm) and the thickness of a grade 1.5 coverslip (170 µm), we obtained tonsil sections that were 10 µm, 20 µm, 30 µm, 35 µm, and 40 µm thick (**Supplementary Fig. 14**). These were stained with Hoechst and y-tubulin conjugated in Alexafluor 555. Gamma-tubulin is punctate and can serve as a useful stain for assessing antibody penetration and image aberration. Z-stacks were acquired for each at 103 nm lateral resolution and 230 nm axial resolution with a 40x/1.2W C-Apochromat water immersion objective lens on a Zeiss LSM980 confocal microscope. We observed punctate gamma-tubulin in all thicknesses up to 35 µm tissue thickness, with uniform intensity along the axial axis (**Supplementary Fig. 14a-d**). However, in the 40 µm thickness, gamma-tubulin appeared to significantly diminish in intensity along the axial axis (**Supplementary figure 14e**). Furthermore, contrast even at the top surface was poorer than thinner samples. This could suggest that standard dewaxing and antigen retrieval protocols are not suitable for thicknesses greater than 35 µm. With Hoechst staining, we also observed severe signal attenuation in the 40 µm. Unlike gamma-tubulin, excitation and emission light penetration may be the issue here, which is well established for short wavelengths.

We then evaluated if certain fluorophores impacted antibody penetration. This is important for CyCIF where the ability to choose different antibody fluorophore combinations is essential. We obtained a primary melanoma and co-stained MART1 conjugated to Alexafluor 647 with other secondary antibodies (Alexafluor 488, Alexafluor 555, Alexafluor 750) (**Supplementary Fig. 15a**) for 8-10 hours at room temperature. We bleached MART1-647 and restained with Alexafluor 647 in a subsequent cycle. **Supplementary Fig. 15b** shows that the MART1 primary conjugate (magenta) penetrated the full thickness of the tissue, as judged by Hoechst staining (turquoise). **Supplementary Fig. 15c-f** shows that all secondary antibodies (magenta) penetrated equally well and showed a similar staining pattern to the MART1 primary conjugate. This demonstrates the ability for secondary antibodies to be used for thick tissue CyCIF. We noted that Alexafluor 750 had lower contrast, however, this can be attributed to the lower sensitivity of detectors in the near infrared spectrum.

While testing multiple primary conjugated antibodies, we observed antibody penetration issues in a subset. Although many immune markers (PD1, CD11c, CD8a, MHC-1, MHC-II; green) showed full depth staining, several tumour and stromal markers (αSMA, PCNA, SOX10; red) only stained the top layer of tissue (**Supplementary Fig. 16**). We questioned whether this was fluorophore dependent, therefore, we repeated staining with the same PCNA clone conjugated to Alexafluor 488 or Alexafluor 750. We noticed there that was a difference in staining pattern; the Alexafluor 488 conjugate stained fewer cells (**Supplementary Fig. 17a**) but showed improved staining penetration (**Supplementary Fig. 17b**). For αSMA, we tried a similar strategy, but using a different fluorophore required a different antibody clone. Unlike PCNA, we did not see an improvement in staining penetration of a blood vessel (**Supplementary Fig. 18**). We reason that antibody penetration is not

uniquely dependent on fluorophore or clone but is influenced by multiple factors and that each antibody must be evaluated using Z-stacks.

3D image acquisition

Tonsil and melanoma image data were collected on a LSM980 Airyscan (Carl Zeiss) equipped with a 405nm, 488nm, 561nm, 647nm, and 750nm laser lines, and 10x/0.45NA air and 40x/1.3NA oil immersion objective lenses. In ZEN 3.7, a 2D overview scan using the 10x objective lens was used to identify regions of interest for higher resolution imaging at 40x in 3D. Images were sampled at 16-bit at 0.14 microns per pixel in X and Y, and 0.28 microns per pixel in Z for approximately 170 or more optical planes. The pinhole size was set to 35 microns. At both resolutions, a focus surface was used to maintain focus. To increase throughput, bidirectional and fast frame scanning was used. Channels were separated into two tracks: track 1 - Hoechst, Alexafluor 555, and Alexafluor 750 (if present). track 2 - Alexafluor 488 and Alexafluor 647. The emission range for Hoechst, Alexafluor 488, Alexafluor 555, Alexafluor 647, and Alexafluor 750 were 380nm-489nm, 499nm-544nm, 579nm-640nm, 660nm-705nm, and 755nm-900nm respectively.

Type I and II collagen were imaged using Second Harmonic Generation (SHG) in a Stellaris 8 DIVE coupled to an Insight X3 multiphoton laser and running LasX. Images were acquired with a 20x/0.75NA multi-immersion lens and sampled at 0.36 microns laterally and 0.95 microns axially. SHG signal was detected using 4Tune Spectra non-descanned HyD detectors and separated from that of Hoechst 33342 using Fluorescence Lifetime Imaging Microscopy (FLIM).

Microscope slides were secured in a slide holder fitted with a spring-loaded clamp, which correspondingly was secured onto the microscope stage in a plateholder.

3D image processing and registration

All channels acquired on the Zeiss LSM980 were processed using Zeiss ZEN LSM Plus Processing to improve signal-to-noise. Channels were background subtracted by removing a fixed constant grey-level from the background. The first cycle was stitched in ZEN using the Hoechst channel as a reference, and all subsequent cycles were registered to this first stitched cycle. Single-field and stitched 3D datasets were imported using Bioformats in MATLAB (Mathworks). First, the X and Y translations were obtained using max projections of the Hoechst nuclei channel. Following this transformation, subsequent cycles were registered in Z. We found that separating the lateral from axial transformations was more accurate than registering X, Y, and Z in one optimization step. We then performed histogram equalization with MATLAB's *histeq()* function and fine-tuned image alignment with elastic deformations using MATLAB's *imregdemons()* function. Lastly, all transformations for each cycle were applied to their corresponding channels. Each channel was saved and appended to a TIFF file and visualized in Imaris 10.0 (Bitplane) as .ims files.

Single-Cell Phenotyping

Manual gating was performed for each marker to differentiate background from true signal. The identified gates for each marker were subsequently used to rescale (similar to batch correction) the single-cell data between 0 and 1, such that the values above 0.5 identified cells expressing the marker and vice versa. The scaled data was subsequently used for phenotyping the cells based on known lineage markers as described previously using the SCIMAP Python package (scimap.xyz).[8] See **Supplementary Table 4** for the detailed marker combinations used to define cell types.

RCN Analysis to Identify Microenvironmental Communities

The Latent Dirichlet allocation (LDA) based recurrent cellular neighbourhood (RCN) was performed using SCIMAP (scimap.xyz)[8] using a k value of 10. The clusters were manually grouped (hierarchical clustering–assisted) into meta-clusters (7 clusters) based on similar microenvironmental community patterns. To validate the RCN assignment, these meta-clusters were overlaid on the original tissue (H&E-stained and fluorescent images). For example, RCN1 generally mapped to the tumour domain, whereas RCN2 mapped to epidermis capturing structural components of the data.

Segmentation of individual 3D cells with Cellpose

Individual 3D cells were segmented from the dense tissue volumes using Cellpose (https://github.com/MouseLand/cellpose),[72] a custom gradient tracking approach which aggregates x-y, y-z, x-z 2D slice cell probability and gradient maps predicted by pretrained 2D segmentation models. The full Cellpose segmentation framework, suitable for a wide range of 3D cell imaging data along with in-depth validation and determination of method applicability will be described elsewhere, see below for the Cellpost workflow specific to this project.

Image preprocessing for Cellpose

The 3D volumes were acquired at voxel resolution of 280 x 140 x 140 nm. For each 3D channel image, we resized the x-y slices by half to obtain isotropic voxels. The raw image intensity, I_{raw}^{ch} was then corrected for uneven illumination, $I_{correct}^{ch} = \overline{I_{raw}^{ch}} \frac{I_{raw}^{ch}}{I_{bg}^{ch}}$ where $\overline{I_{raw}^{ch}}$ is the mean image intensity and I_{bg}^{ch} an estimation of the background illumination obtained by downsampling the image by a factor of 8, Gaussian smoothing with sigma = 5 and resizing back to the original image dimensions. $I_{correct}^{ch}$ was then contrast-stretched to a range of 0-1, clipping any intensities less than the 2nd percentile to 0 and any greater than the 99.8th percentile to 1. Cellpose uses a single channel cytoplasmic and nuclear signal for two-color based cell segmentation. The mean of the intensity-normalized, background-corrected HLA-AB, CD3E, CD11b, and β-actin channels was used as the cytoplasmic signal. DAPI was used as the nucleus signal. Both cytoplasmic and nucleus signals underwent a further round of background correction and contrast stretching as described above before being concatenated to form the input RGB volume image.

Running Cellpose 2D

The RGB volume was input slice-by-slice to Cellpose 2D in three different orientations; x-y, x-z, y-z to obtain three stacks of cell probability and 2D gradients. The performance of Cellpose depends on appropriate setting of the diameter parameter which relates to the size of the cells to be segmented. As the appearance of the cells may vary depending on orientation, we conduct a parameter screen with diameter = [10,100] at increments of 5 using the mid-slice for each orientation. At each diameter we compute the 'sharpness' of the predicted gradient map as the mean of the image variance evaluated over a local 5x5 pixel window in both 'x' and 'y' gradient directions. The diameter maximizing the variance after a moving average smoothing with window size of 3 was used to run Cellpose 2D on the remaining slices in the orientation. The raw cell probability output, P from Cellpose are the inputs to a sigmoid centered at zero, $1/(1+e^{-P})$.This means the probabilities vary predominantly linearly in the range -6 to +6 and this reduces the distinction between foreground and background. Thus, we clip the probabilities to the range [-88.72, 88.72] (to prevent overflow or underflow in float32) and convert back to a normalized probability value in the range 0-1 by evaluating the sigmoid, $1/(1+e^{-P})$. The probabilities from all 3 orientations are combined into one by averaging. Similarly, the 2D gradients are Gaussian smoothed with sigma=1 voxel and combined into a single 3D gradient map. Gradients are then normalized to be unit length. Lastly, we perform 3-level Otsu thresholding on the combined probability map and use the lower threshold to define the foreground binary voxels for gradient tracking.

Aggregating Cellpose 2D predictions

The volume was divided into subvolumes of (256, 512, 512) with 25% overlap. Within each subvolume we run gradient descent with momentum for 200 iterations, momenta, $\mu = 0.98$, step size $\delta = 1$ to propagate the position of foreground pixels towards its final attractor in the 3D gradient map.

$$\left(x_i^{t+1}, y_i^{t+1}, z_i^{t+1}\right) \leftarrow \left(x_i^t, y_i^t, z_i^t\right) + \frac{1}{\delta+\mu}\left(\delta \cdot \nabla\left(x_i^t, y_i^t, z_i^t\right) + \mu \cdot \nabla\left(x_i^{t-1}, y_i^{t-1}, z_i^{t-1}\right)\right)$$

Here (x_i^t, y_i^t, z_i^t) denotes the coordinate of foreground voxel i at iteration number t, μ the momentum ranging from 0-1, δ the step size and ∇ is the gradient map. Nearest neighbor interpolation is used, thus (x_i^t, y_i^t, z_i^t) is always integer valued. Gradient tracking of all subvolumes are conducted in parallel using multiprocessing. The final coordinate positions from all subvolumes are compiled. We then build a volume count map where voxels mapping to the same final coordinate adds +1 to the count. The count map is Gaussian smoothed with sigma=1 and binarized using the mean value as the threshold. Connected component analysis identifies the unique cell as clusters where foreground voxels have been mapped to the same cell. Transferring this labelling to initial voxel positions $\left(x_i^{t=0}, y_i^{t=0}, z_i^{t=0}\right)$ generates the individual 3D cell segmentations.

Postprocessing 3D cell segmentations

Small individual cell masks (<1000 voxels$^3 \approx 20\mu m^3$) were first removed. We also removed all cell masks that do not agree with the Cellpose predicted 3D gradient map. This is done by computing the

3D heat diffusion gradient map given the computed 3D cell segmentations and computing the mean squared error (MSE) with the input combined Cellpose 3D gradient map for each cell. Cells with MSE > 0.8 were discarded. Cells that are implausibly large, with volume greater than the mean volume $\pm$ 5 standard deviations were also discarded.

For the remainder cells, we run a label propagation[73] to enforce that each segmented cell mask comprises only a single connected component and to denoise the masks. This is done for each cell mask, M_i, by cropping a subvolume, V_i, the size of its bounding box padded isotropically by 25 voxels. Each unique cell region is represented as a positive integer label. Every label in V_i is encoded using a one-hot encoding scheme to create a binary column for each unique label. This generates a label matrix, $L_i \in \mathbb{R}^{N \times p+1}$ for V_i, where N is the total number of voxels and p the number of unique labels in V_i and one additional label for background. We then construct the affinity matrix, A, as a weighted sum ($\alpha = 0.25$) of an affinity matrix based on the intensity difference in the cytoplasmic signal between 8-connected voxel neighbors, $A_{intensity}$, and one based on the connectivity alone, $A_{laplacian}$; $A = \alpha A_{intensiy} + (1-\alpha)A_{laplacian}$. $A_{intensity} = \begin{cases} e^{-D_{intensity}/(2\mu(D_{intensity})^2)} & i \neq j \\ 1 & i = j \end{cases}$ where $D_{intensity}$ is the pairwise absolute difference matrix between two neighboring voxels i and j. $A_{laplacian} = \begin{cases} e^{-D^2_{laplacian}/(2\mu(D_{laplacian})^2)} & i \neq j \\ 1 & i = j \end{cases}$ where $D_{laplacian}$ is the graph Laplacian with a value of 1 if a voxel i is a neighbor of voxel j, and 0 otherwise. $\mu(D)$ denotes the mean value of the entries of matrix D. The iterative label propagation is

$$z \in \mathbb{R}^{N \times p}$$

$$z^{t=0} = \mathbf{0}$$

$$z^{t+1} \leftarrow (1-\gamma)A\, z^t + (\gamma)L,$$

where t is the interation number, $\mathbf{0}$, denotes the empty vector and γ is a 'clamping' factor that controls the extent the original labeling is preserved. We set $\gamma = 0.01$. We run the propagation for 25 iterations. The final z is normalized using the softmax operation and argmax is used to obtain the final labels. The refined cell mask, M_i^{refine} is defined by all voxels where z has the same cell label i. All postprocessing steps were implemented using parallel multiprocessing iterating over individual cells.

Statistical Tests

All statistical tests were performed using MATLAB's *ttest2* implementation of the two-sample t-test without assuming equal variances and significance value of p<0.05.

Figures and Legends

Figure 1

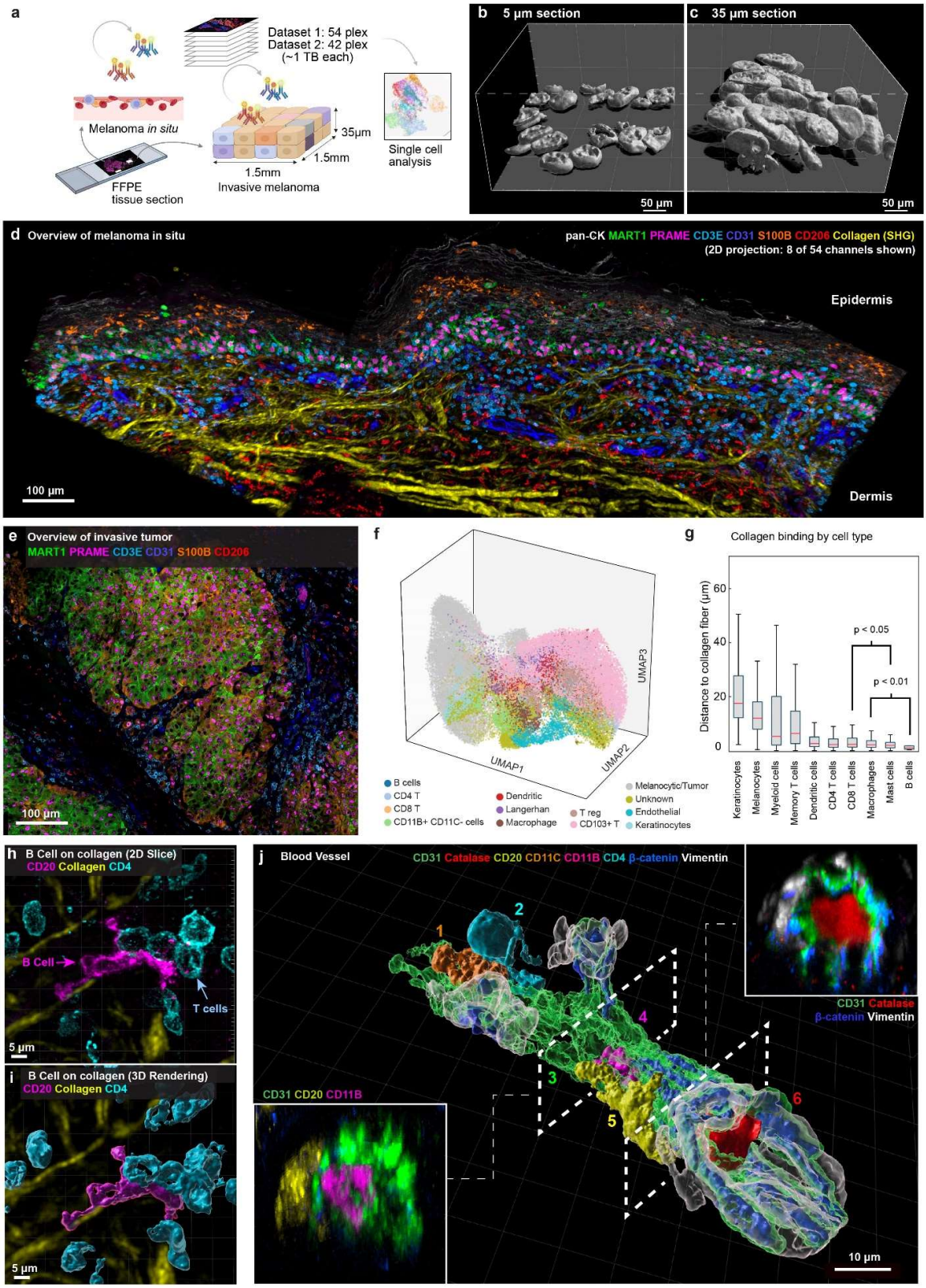

Figure 1: Demonstrating the need for thick tissue sections using 3D CyCIF and SHG imaging: **a,** Schematic of 3D CyCIF data collection, dimension and size. **b,c,** Surface rendering illustrates the

nuclei volume of (**b**) 5 µm and (**c**) 35 µm tissue sections. Scale bars, 50 µm. **d,** Maximum intensity projection of multi modal image integrating 3D CyCIF with second harmonic signal of collagen highlighting the melanoma in-situ region (MIS). Scale bar, 100 µm. **e**, Maximum intensity projection of 3D CyCIF imaging of invasive margin from the same patient as panel d. Scale bar, 100 µm. **f**, UMAP rendering of all cell types analyzed in Dataset 1, **g,** Tukey box plot illustrating the distances between collagen fibres and different cell types. Statistical significance was assessed using one sided unpaired student's *t-test*. Centre line, median; box limits, upper and lower quartiles; whiskers, minimum and maximum after removing outliers. **h,i,** Representative $CD20^+$ B cell (magenta) with elongated morphology interacting closely with collagen fibres (yellow), as a maximum intensity projection (**h**) or surface rendering (**i**) of the same panel. Scale bars, 5 µm. **j,** Surface rendering of a segment of an intact blood vessel within the MIS region. Dashed lines demarcate cutting planes for cross-sectional views (insets), illustrating the capability to distinguish between internal components of the blood vessel (CD11B+ cell - magenta; red blood cell - red) and external, fully intact B cell (yellow). Scale bar, 10 µm.

Figure 2

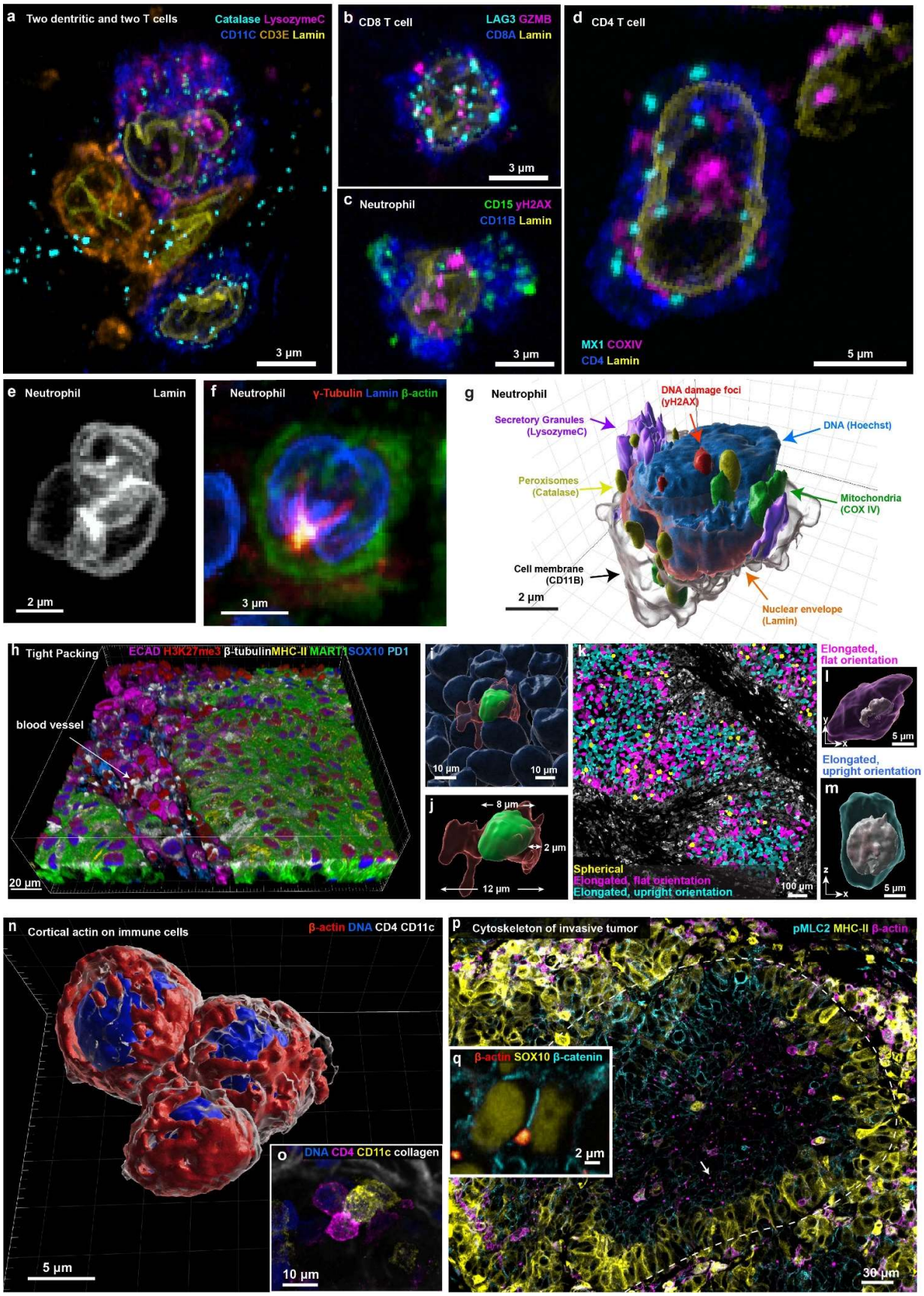
a Two dentritic and two T cells
Catalase LysozymeC
CD11C CD3E Lamin
3 µm
b CD8 T cell
LAG3 GZMB
CD8A Lamin
3 µm
c Neutrophil
CD15 γH2AX
CD11B Lamin
3 µm
d CD4 T cell
MX1 COXIV
CD4 Lamin
5 µm
e Neutrophil
Lamin
2 µm
f Neutrophil
γ-Tubulin Lamin β-actin
3 µm
g Neutrophil
DNA damage foci (γH2AX)
Secretory Granules (LysozymeC)
DNA (Hoechst)
Peroxisomes (Catalase)
Mitochondria (COX IV)
Cell membrane (CD11B)
2 µm
Nuclear envelope (Lamin)
h Tight Packing
ECAD H3K27me3 β-tubulin MHC-II MART1 SOX10 PD1
blood vessel
20 µm
i
10 µm
10 µm
j
8 µm
2 µm
12 µm
k
Spherical
Elongated, flat orientation
Elongated, upright orientation
100 µm
Elongated, flat orientation
l
5 µm
Elongated, upright orientation
m
5 µm
n Cortical actin on immune cells
β-actin DNA CD4 CD11c
5 µm
o
DNA CD4 CD11c collagen
10 µm
p Cytoskeleton of invasive tumor
pMLC2 MHC-II β-actin
30 µm
q
β-actin SOX10 β-catenin
2 µm

Figure 2: 3D CyCIF imaging reveals intracellular features and tumour microenvironment characteristics in melanoma: a-g, Selected channels of 54 plex 3D CyCIF images of cells found in the dermis of the MIS (full marker assignment in **Supplementary Table 4**) **a,** Two dendritic cells and two T cells highlighting intracellular catalase and lysozyme C. **b,** CD8 T cell highlighting punctate LAG3 on the cell surface and GZMB in secretory granules. **c,** Neutrophil highlighting γH2AX^{+} foci in the nucleus. **d,** CD4 T cell highlighting COX4 in mitochondria and MX1 in biomolecular condensates. **e-g,** Tri-lobe nucleus of CD11B+ neutrophil, highlighting lamin (**e**), the microtubule organising centre (**f**), and a 3D surface rendering of diverse intracellular organelles in a single neutrophil (**g**). **h-j,** FOVs capturing the boundary of a vertically growing tumour, highlighting the densely packed nature of the tissue at low-resolution (**h**) and high-resolution renderings of individual cell (**i** & **j**). **k,** Mask plots overlaid on the vertical growth phase melanoma region, highlighting spherical cells in yellow and elongated cells in magenta and cyan. Scale bar, 100 μm. **l,m**, Surface renderings of selected cells from **k**. **n**, surface rendering of 3 immune cells shown in o. Cortial actin shown in red under immune marker in grey. Scale bar, 5 μm **o**, Volumetric rendering of two T cells (magenta) and one dendritic cell (yellow) shown in n. Scale bar, 10 μm, **p,q,** An orthogonal slice of a vertical growth phase melanoma region, highlighting the punctate nature of **β**-actin in tumour cells and the generally elevated expression levels of **β**-actin in immune cells, alongside graded pMLC2 expression (**p**). Scale bar, 30 μm; high resolution inset of **β**-actin puncta in SOX10^{+} tumour cell (**q**). Scale bar, 2 μm.

Figure 3

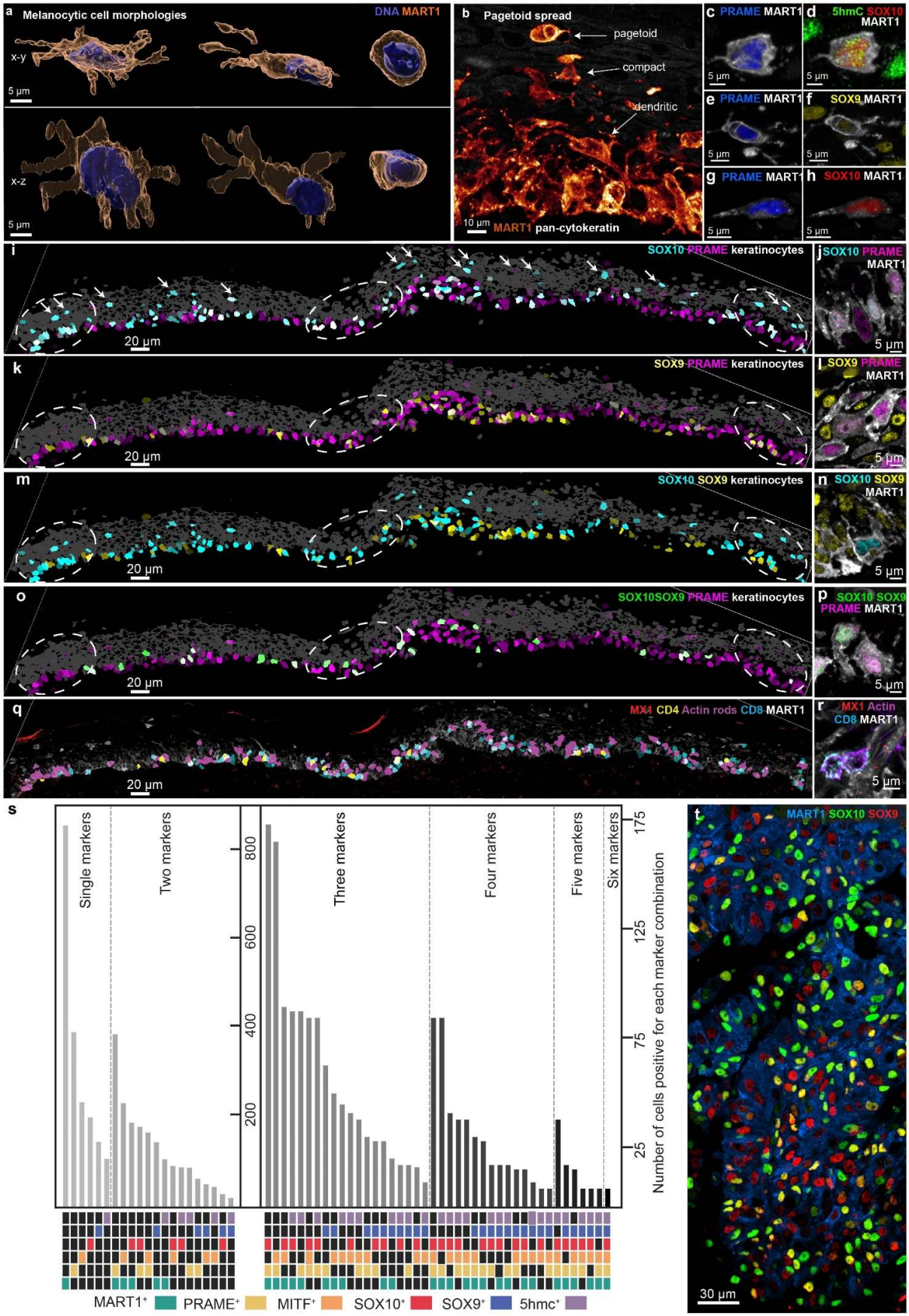
a Melanocytic cell morphologies
DNA MART1
x-y
x-z
5 µm
b Pagetoid spread
pagetoid
compact
dendritic
10 µm
MART1 pan-cytokeratin
c PRAME MART1
d 5hmC SOX10 MART1
e PRAME MART1
f SOX9 MART1
g PRAME MART1
h SOX10 MART1
i SOX10 PRAME keratinocytes
j SOX10 PRAME MART1
k SOX9 PRAME keratinocytes
l SOX9 PRAME MART1
m SOX10 SOX9 keratinocytes
n SOX10 SOX9 MART1
o SOX10SOX9 PRAME keratinocytes
p SOX10 SOX9 PRAME MART1
q MX1 CD4 Actin rods CD8 MART1
r MX1 Actin CD8 MART1
20 µm
s
Single markers
Two markers
Three markers
Four markers
Five markers
Six markers
Number of cells positive for each marker combination
MART1+ PRAME+ MITF+ SOX10+ SOX9+ 5hmc+
t MART1 SOX10 SOX9
30 µm

Figure 3: Melanocyte morphologies, lineage marker expression, and cellular interactions in the melanocytic intraepidermal compartment: a, Surface-rendered melanocytes within the MIS, illustrating variations in conventional dendritic-like and rounded morphologies. Scale bars, 5 µm. **b,** A representative FOV showcasing the transition of melanocyte morphology from dendritic-like at the DEJ to compact (bottom), and ultimately rounded, during the pagetoid spread within the epidermis (top). Scale bars, 10 µm. **c-h**, Representative examples of PRAME- and MART1-expressing pagetoid spread cells showing different expression levels of 5hMC, SOX9 and SOX10. Markers as indicated on each panel. Scale bars, 5 µm, **i-p**, Images of the MIS. Left column: segmentation masks coloured by marker intensity and brightness representing mean expression level. Masks in grey denote the positions of keratinocytes; dashed circles denote IFN-rich domains. Markers as indicated on each panel. Right column: high-resolution immunofluorescence images of the same markers per row. **q,r,** Images as in **l-p** but with magenta denoting cells containing nuclear actin rods. **s,** Bar graph showing the number of melanocytic cells in the MIS positive for each of 63 combinations of marker proteins. MART1 (green), PRAME (yellow), MITF (orange), SOX10 (red), SOX9 (blue), and 5hmc (violet). Note different y-axes. **t**, Maximum projection of a region from the vertical growth phase showing variability of SOX9 (red) and SOX10 (green) expression. Scale bar, 30 µm.

Figure 4

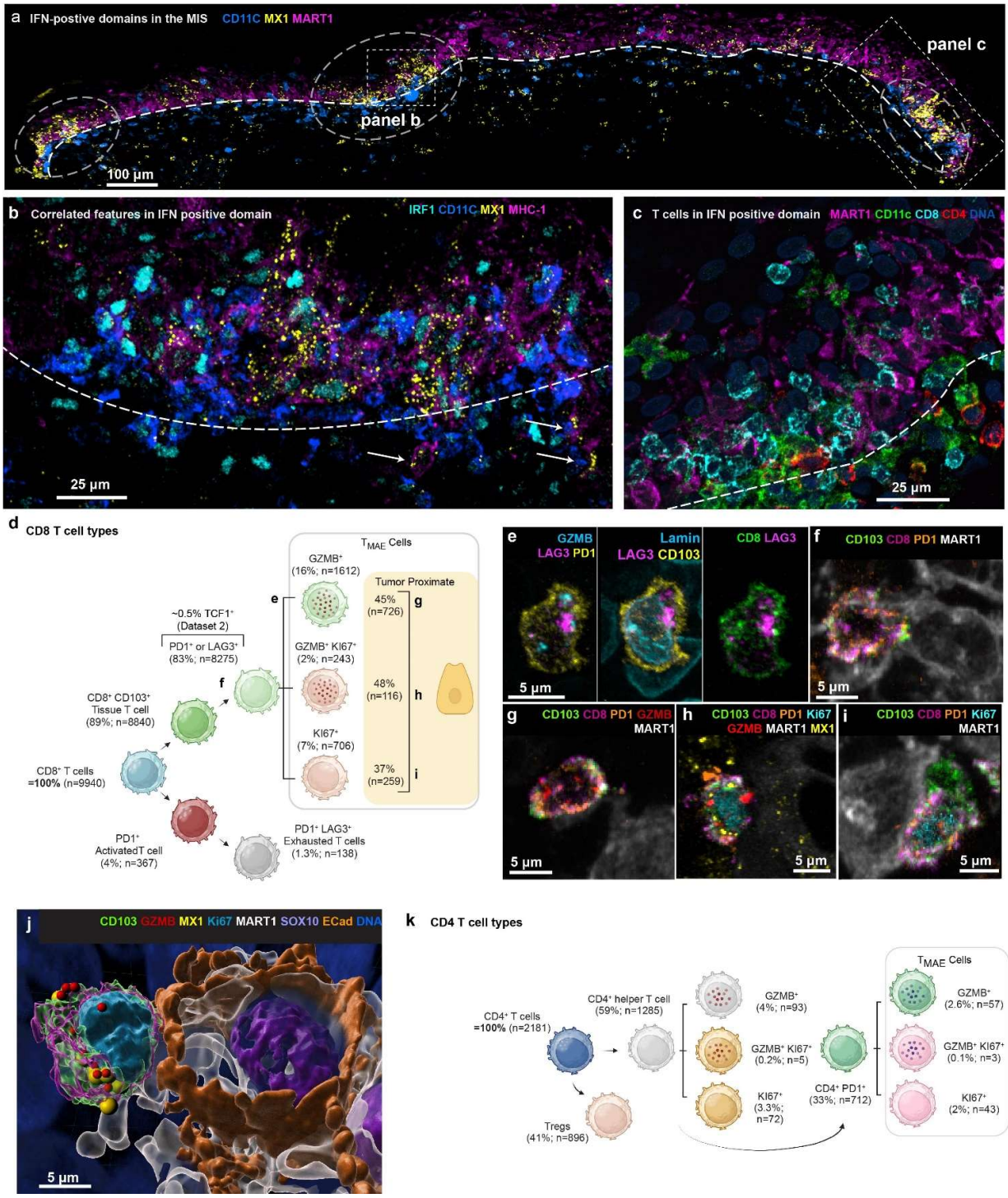

Figure 4: Spatial analysis of IFN-rich domains: a, Three selected channels of 54-plex CyCIF image of MIS (dataset 2); a single image plane from the middle of the specimen is shown. IFN-rich domains denoted by dashed circles. DEJ denoted by white dashed line. Scale bar 100 µm. **b,** Magnified view of inset from panel **a** showing coincident nuclear localization of IRF1, expression of MX1, and MHC-1 upregulation. DEJ denoted by white dashed line. White arrowheads indicate

invading melanocytic cells into dermis. Scale bars, 50 µm. **c,** Enlarged inset from panel (**a**) showing diversity of immune cells crossing the DEJ. DEJ denoted by white dashed lines. **d,** Hierarchical tree diagram showing proportions of CD8 T sublineages including T_{MAE} . Yellow shaded box indicates immune cells next to tumour cells, **e-i,** representative examples of cells denoted in **d**. Marker colours indicated in panels. **j**, Surface rendering of panel h. Scale bars, 5 µm. **k**, Hierarchical tree diagram showing proportions of CD4 T sublineages.

Figure 5

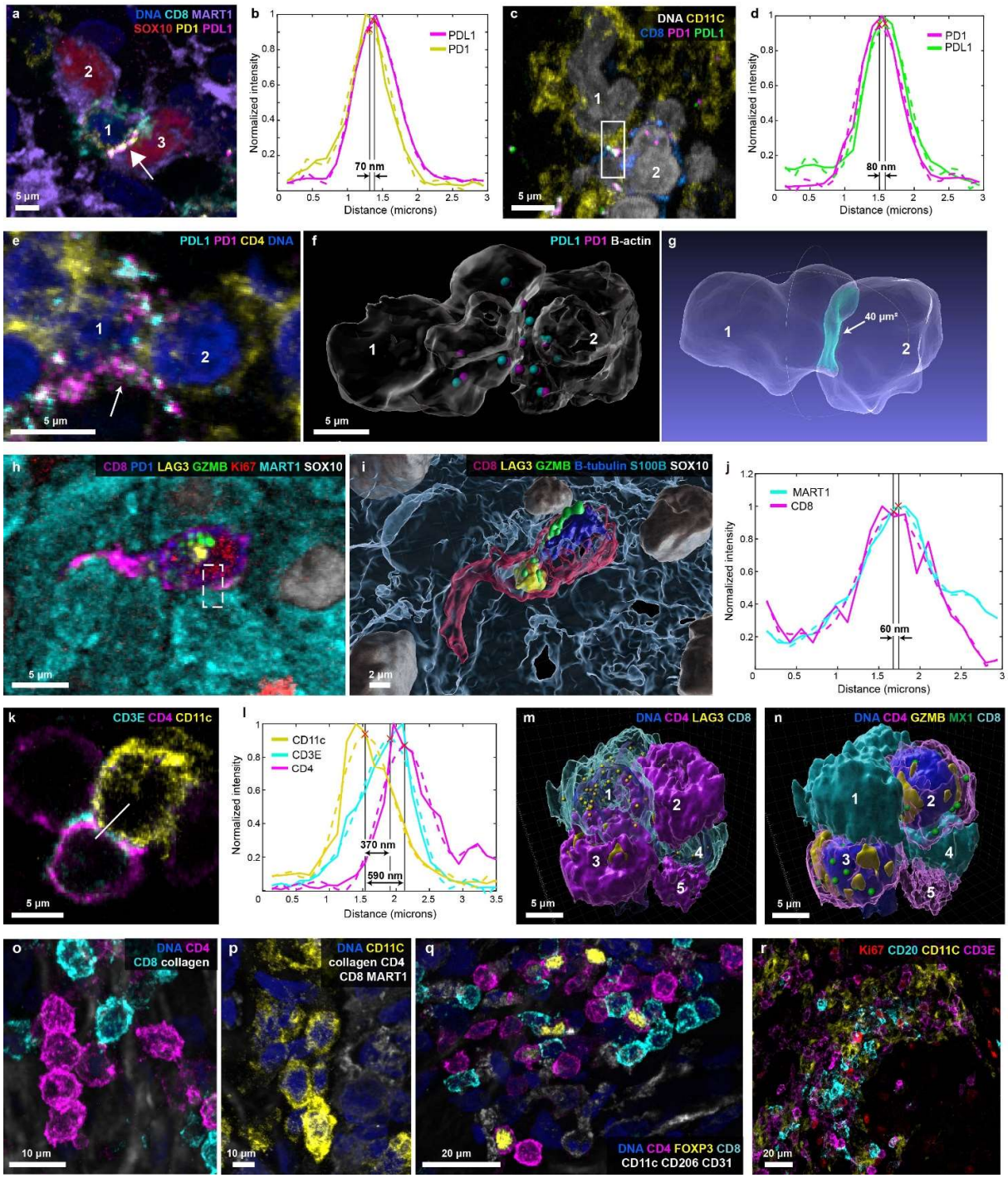

Figure 5 Cell-cell interactions: Selected fields of view and surface renderings from dataset 2. **a,** A single image plane of a PD1⁺ dendritic cell (cell 1) interacting with two MART1⁺ tumour cells. White arrow denotes juxtacrine PD1-PDL1 interaction. Scale bar 5 µm. **b**, Line integral of interaction of cells 1 and 3 in **a**. **c-d,** A dendritic cell (cell 1) interacting with a CD8⁺ T cell. Box indicates region of line integral shown in **d**. **e-g,** Representations of two CD4⁺ T cells interacting expressing PD1 and

PDL1 as a maximum projection, **e**, surface rendering where colocalized PD1 and PDL1 is shown as spheres, **f**, and transparent surface mesh showing contact area, **g, h-j,** Representations of a T_{PEX} cell from the invasive margin as a maximum projection, **h**, surface rendering, **i**, and line integral across membrane shown in region marked by white dashed box in (**h), j. k,l,** The image underscores a conventional direct interaction between a CD4 helper T cell (magenta) and a dendritic cell (yellow). The degree of direct interaction can be further evaluated by line integral computation and is presented in (**l**). **m,** Surface rendering of five immune cells involving Type II interactions among three $CD4^+$ helper T cells (magenta-opaque) and two $CD8^+$ T cells (cyan-transparent). **n,** Same rendering with transparency reversed. Also shown, MX1 biomolecular condensates (green), globular $GZMB^+$ (yellow in **n**) $CD4^+$ T cells and punctate LAG3 (yellow) on the membranes of $CD8^+$ T cells. Spacing between opposed membranes is <1.5 µm and contact area is ~20µm^2. Scale bars, 5 µm. **o-q,** Examples of Type III interactions, (lymphonets) involving $CD4^+$ $CD8^+$ dendritic cells. These networks are characterised by cell-cell interactions involving immediate contact through relatively small membrane domains and a loosely packed arrangement. **r,** Stroma in the vicinity of the invasive melanoma showing neighbourhoods rich in $CD20^+$ B cells, $CD11C^+$ dendritic cells, $CD3E^+$ T cells but without the clusters of proliferating Ki-67^+ cells characteristic of mature germinal centres.

Figure 6

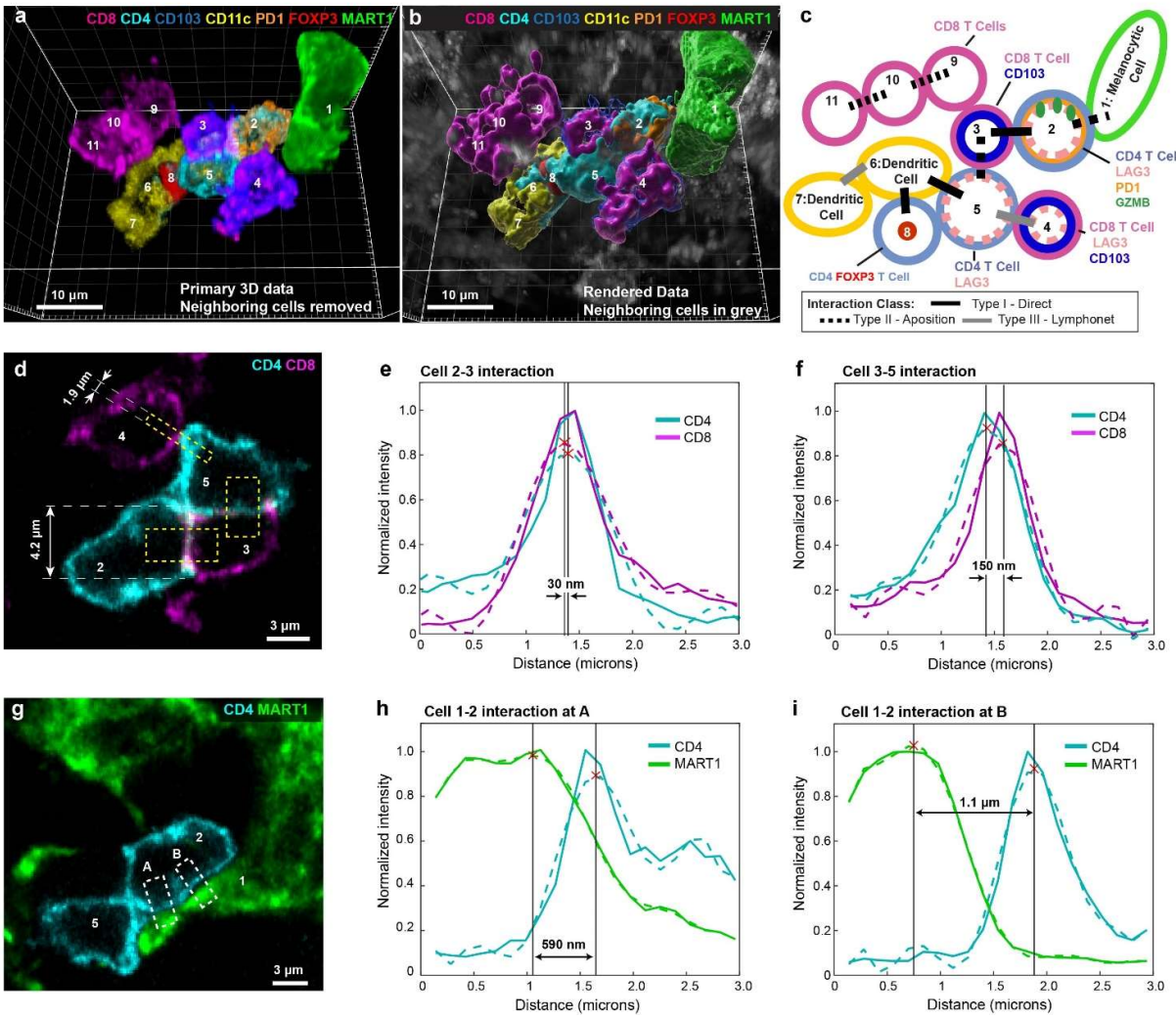

Figure 6: Multivalent immune cell niche defined by membrane-membrane interaction. a-c, 11 cells from the MIS lying in proximity to the DEJ, shown as primary data (**a**), 3D surface renderings (**b**), and as a schematic representation of three Type I, four Type II, and two Type III interactions inferred from line integrals in single-plane images (**c**). Scale bars, 10 µm. **d,** A cross-sectional slice of the two $CD8^+$ T cells and two $CD4^+$ featured in (**a**), depicting the direct engagement of cell membranes. Scale bar 3 µm. **e,f,** A line integral plot depicting CD4 and CD8 average expression within the bottom boxed region of **d** (**e**) or right boxed region of **d** (**f**). **g-i,** A Type II interaction between a $MART1^+$ tumour cell and $CD4^+$ T cells, as a representative image (**g**) and line integrals for the interaction between cells 1-2 at region A (**h**) and B (**i**). Scale bars, 3 µm.

Supplementary Videos

Supplementary Video 1: Surface rendering of Hoechst stained 5 and 35 micron thick serial sections from primary melanoma. 3D rendering from Bitplane Imaris 10.0.

Supplementary Video 2: Surface rendering of an intact blood vessel (green) from the MIS region with B cell (yellow), red blood cell (red), and neutrophil (pink). 3D rendering from Bitplane Imaris 10.0.

Supplementary Video 3: Volumetric rendering of packed tumor cells from the invasive margin. Rendering from Bitplane Imaris 10.0. Marker colors as indicated.

Supplementary Video 4: Surface rendering of CD4 (magenta) and CD8 (blue) positive T cells with LAG3 (yellow spheres), MX1 (green sphere), and GZMB (yellow blobs). Rendering from Bitplane Imaris 10.0.

Supplementary Video 5: Surface rendering of 1 melanocytic cell (green) and 10 interacting immune cells comprising of CD4 T cells (blue), CD8 T cells (magenta), and dendritic cells (yellow) from the MIS region. Rendering from Bitplane Imaris 10.0.

Supplemental Tables

Supplementary Table 1: Sample metadata and HTAN identifiers.

Supplementary Table 2: Antibody panel used for dataset 1.

Supplementary Table 3: Antibody panel used for dataset 2.

Supplementary Table 4: Marker combinations used to define distinct cell types and lineages.

References

1. Rozenblatt-Rosen, O. *et al.* The Human Tumor Atlas Network: Charting Tumor Transitions across Space and Time at Single-Cell Resolution. *Cell* **181**, 236–249 (2020).

2. Hickey, J. W. *et al.* Spatial mapping of protein composition and tissue organization: a primer for multiplexed antibody-based imaging. Preprint at http://arxiv.org/abs/2107.07953 (2021).

3. Lin, J.-R. *et al.* Highly multiplexed immunofluorescence imaging of human tissues and tumors using t-CyCIF and conventional optical microscopes. *eLife* **7**, (2018).

4. Prasad, A. & Alizadeh, E. Cell Form and Function: Interpreting and Controlling the Shape of Adherent Cells. *Trends Biotechnol* **37**, 347–357 (2019).

5. Clark, W. H. *et al.* A study of tumor progression: The precursor lesions of superficial spreading and nodular melanoma. *Human Pathology* **15**, 1147–1165 (1984).

6. Gaglia, G. *et al.* Lymphocyte networks are dynamic cellular communities in the immunoregulatory landscape of lung adenocarcinoma. *Cancer Cell* **41**, 871-886.e10 (2023).

7. Rao, A., Barkley, D., França, G. S. & Yanai, I. Exploring tissue architecture using spatial transcriptomics. *Nature* **596**, 211–220 (2021).

8. Nirmal, A. J. *et al.* The Spatial Landscape of Progression and Immunoediting in Primary Melanoma at Single-Cell Resolution. *Cancer Discovery* **12**, 1518–1541 (2022).

9. Kaufmann, C. *et al.* The role of cyclin D1 and Ki-67 in the development and prognostication of thin melanoma. *Histopathology* **77**, 460–470 (2020).

10. Sadjadi, Z., Zhao, R., Hoth, M., Qu, B. & Rieger, H. Migration of Cytotoxic T Lymphocytes in 3D Collagen Matrices. *Biophysical Journal* **119**, 2141–2152 (2020).

11. Van Goethem, E., Poincloux, R., Gauffre, F., Maridonneau-Parini, I. & Le Cabec, V. Matrix Architecture Dictates Three-Dimensional Migration Modes of Human Macrophages: Differential

Involvement of Proteases and Podosome-Like Structures. *The Journal of Immunology* **184**, 1049–1061 (2010).

12. Kuczek, D. E. *et al.* Collagen density regulates the activity of tumor-infiltrating T cells. *j. immunotherapy cancer* **7**, 68 (2019).

13. Pruitt, H. C. *et al.* Collagen fiber structure guides 3D motility of cytotoxic T lymphocytes. *Matrix Biology* **85–86**, 147–159 (2020).

14. Muller, W. A. Getting Leukocytes to the Site of Inflammation. *Vet Pathol* **50**, 7–22 (2013).

15. Willsmore, Z. N. *et al.* B Cells in Patients With Melanoma: Implications for Treatment With Checkpoint Inhibitor Antibodies. *Front Immunol* **11**, 622442 (2021).

16. Viana, M. P. *et al.* Integrated intracellular organization and its variations in human iPS cells. *Nature* **613**, 345–354 (2023).

17. Wu, Y., Pegoraro, A. F., Weitz, D. A., Janmey, P. & Sun, S. X. The correlation between cell and nucleus size is explained by an eukaryotic cell growth model. *PLoS Comput Biol* **18**, e1009400 (2022).

18. Chen, H., Li, D. & Bar-Joseph, Z. SCS: cell segmentation for high-resolution spatial transcriptomics. *Nat Methods* **20**, 1237–1243 (2023).

19. Yamaguchi, H. & Condeelis, J. Regulation of the actin cytoskeleton in cancer cell migration and invasion. *Biochimica et Biophysica Acta (BBA) - Molecular Cell Research* **1773**, 642–652 (2007).

20. Georgouli, M. *et al.* Regional Activation of Myosin II in Cancer Cells Drives Tumor Progression via a Secretory Cross-Talk with the Immune Microenvironment. *Cell* **176**, 757-774.e23 (2019).

21. Blauth, E., Kubitschke, H., Gottheil, P., Grosser, S. & Käs, J. A. Jamming in Embryogenesis and Cancer Progression. *Frontiers in Physics* **9**, (2021).

22. Jackett, L. A. & Scolyer, R. A. A Review of Key Biological and Molecular Events Underpinning Transformation of Melanocytes to Primary and Metastatic Melanoma. *Cancers (Basel)* **11**, 2041 (2019).

23. Smoller, B. R. Histologic criteria for diagnosing primary cutaneous malignant melanoma. *Mod Pathol* **19**, S34–S40 (2006).

24. Chudnovsky, Y., Khavari, P. A. & Adams, A. E. Melanoma genetics and the development of rational therapeutics. *J Clin Invest* **115**, 813–824 (2005).

25. Hodis, E. *et al.* A Landscape of Driver Mutations in Melanoma. *Cell* **150**, 251–263 (2012).

26. Lian, C. G. *et al.* LOSS OF 5-HYDROXYMETHYLCYTOSINE IS AN EPIGENETIC HALLMARK OF MELANOMA. *Cell* **150**, 1135–1146 (2012).

27. Lezcano, C., Jungbluth, A. A., Nehal, K. S., Hollmann, T. J. & Busam, K. J. PRAME Expression in Melanocytic Tumors. *Am J Surg Pathol* **42**, 1456–1465 (2018).

28. Gassenmaier, M. *et al.* Diffuse PRAME Expression Is Highly Specific for Thin Melanomas in the Distinction from Severely Dysplastic Nevi but Does Not Distinguish Metastasizing from Non-Metastasizing Thin Melanomas. *Cancers* **13**, 3864 (2021).

29. Boiko, A. D. *et al.* Human melanoma-initiating cells express neural crest nerve growth factor receptor CD271. *Nature* **466**, 133–137 (2010).

30. Kloc, M. *et al.* New Insights into Cellular Functions of Nuclear Actin. *Biology (Basel)* **10**, 304 (2021).

31. Sehgal, P. B. *et al.* Murine GFP-Mx1 forms nuclear condensates and associates with cytoplasmic intermediate filaments: Novel antiviral activity against VSV. *J Biol Chem* **295**, 18023–18035 (2021).

32. Sehgal, P. B. Metastable biomolecular condensates of interferon-inducible antiviral Mx-family GTPases: A paradigm shift in the last three years. *J Biosci* **46**, 72 (2021).

33. Kim, Y. J. *et al.* Melanoma dedifferentiation induced by IFN-γ epigenetic remodeling in response to anti-PD-1 therapy. *J Clin Invest* **131**, e145859, 145859 (2021).

34. Watanabe, R. *et al.* Human skin is protected by four functionally and phenotypically discrete populations of resident and recirculating memory T cells. *Sci Transl Med* **7**, 279ra39 (2015).

35. Utzschneider, D. T. *et al.* Early precursor T cells establish and propagate T cell exhaustion in chronic infection. *Nat Immunol* **21**, 1256–1266 (2020).

36. Burger, M. L. *et al.* Antigen dominance hierarchies shape TCF1+ progenitor CD8 T cell phenotypes in tumors. *Cell* **184**, 4996-5014.e26 (2021).

37. Miller, B. C. *et al.* Subsets of exhausted CD8+ T cells differentially mediate tumor control and respond to checkpoint blockade. *Nat Immunol* **20**, 326–336 (2019).

38. Kallies, A., Zehn, D. & Utzschneider, D. T. Precursor exhausted T cells: key to successful immunotherapy? *Nat Rev Immunol* **20**, 128–136 (2020).

39. Lin, L. *et al.* Granzyme B secretion by human memory CD4 T cells is less strictly regulated compared to memory CD8 T cells. *BMC Immunol* **15**, 36 (2014).

40. Lin, W. *et al.* Human CD4 cytotoxic T lymphocytes mediate potent tumor control in humanized immune system mice. *Commun Biol* **6**, 1–13 (2023).

41. Dustin, M. L. The immunological synapse. *Cancer Immunol Res* **2**, 1023–1033 (2014).

42. Cabrita, R. *et al.* Tertiary lymphoid structures improve immunotherapy and survival in melanoma. *Nature* **577**, 561–565 (2020).

43. Werner, F. *et al.* A Standardized Analysis of Tertiary Lymphoid Structures in Human Melanoma: Disease Progression- and Tumor Site-Associated Changes With Germinal Center Alteration. *Front Immunol* **12**, 675146 (2021).

44. Huang, F., Santinon, F., Flores González, R. E. & del Rincón, S. V. Melanoma Plasticity: Promoter of Metastasis and Resistance to Therapy. *Front Oncol* **11**, 756001 (2021).

45. Oyler-Yaniv, A. *et al.* A Tunable Diffusion-Consumption Mechanism of Cytokine Propagation Enables Plasticity in Cell-to-Cell Communication in the Immune System. *Immunity* **46**, 609–620 (2017).

46. Palla, G. *et al.* Squidpy: a scalable framework for spatial omics analysis. *Nat Methods* **19**, 171–178 (2022).

47. Chen, Z., Soifer, I., Hilton, H., Keren, L. & Jojic, V. Modeling Multiplexed Images with Spatial-LDA Reveals Novel Tissue Microenvironments. *J Comput Biol* **27**, 1204–1218 (2020).

48. Wallace, W., Schaefer, L. H. & Swedlow, J. R. A Workingperson's Guide to Deconvolution in Light Microscopy. *BioTechniques* **31**, 1076–1097 (2001).

49. Fish, K. N. Total Internal Reflection Fluorescence (TIRF) Microscopy. *CP Cytometry* **50**, (2009).

50. Axelrod, D., Thompson, N. L. & Burghardt, T. P. Total internal reflection fluorescent microscopy. *Journal of Microscopy* **129**, 19–28 (1983).

51. Egger, M. D. & Petráň, M. New Reflected-Light Microscope for Viewing Unstained Brain and Ganglion Cells. *Science* **157**, 305–307 (1967).

52. Wilson, T. Resolution and optical sectioning in the confocal microscope: PROPERTIES OF THE FLUORESCENT CONFOCAL MICROSCOPE. *Journal of Microscopy* **244**, 113–121 (2011).

53. Wilson, T. Optical sectioning in confocal fluorescent microscopes. *Journal of Microscopy* **154**, 143–156 (1989).

54. Murray, J. M., Appleton, P. L., Swedlow, J. R. & Waters, J. C. Evaluating performance in three-dimensional fluorescence microscopy. *J Microsc* **228**, 390–405 (2007).

55. Denk, W., Strickler, J. H. & Webb, W. W. Two-Photon Laser Scanning Fluorescence Microscopy. *Science* **248**, 73–76 (1990).

56. Campagnola, P. J. *et al.* Three-Dimensional High-Resolution Second-Harmonic Generation Imaging of Endogenous Structural Proteins in Biological Tissues. *Biophysical Journal* **82**, 493–508 (2002).

57. Campagnola, P. J., Wei, M., Lewis, A. & Loew, L. M. High-Resolution Nonlinear Optical Imaging of Live Cells by Second Harmonic Generation. *Biophysical Journal* **77**, 3341–3349 (1999).

58. Zipfel, W. R. *et al.* Live tissue intrinsic emission microscopy using multiphoton-excited native fluorescence and second harmonic generation. *Proc. Natl. Acad. Sci. U.S.A.* **100**, 7075–7080 (2003).

59. Ghose, S. *et al. Human Digital Twin: Automated Cell Type Distance Computation and 3D Atlas Construction in Multiplexed Skin Biopsies*. http://biorxiv.org/lookup/doi/10.1101/2022.03.30.486438 (2022) doi:10.1101/2022.03.30.486438.

60. Kuett, L. *et al.* Three-dimensional imaging mass cytometry for highly multiplexed molecular and cellular mapping of tissues and the tumor microenvironment. *Nat Cancer* **3**, 122–133 (2022).

61. Ghose, S. *et al.* 3D reconstruction of skin and spatial mapping of immune cell density, vascular distance and effects of sun exposure and aging. *Commun Biol* **6**, 718 (2023).

62. Lin, J.-R. *et al.* Multiplexed 3D atlas of state transitions and immune interaction in colorectal cancer. *Cell* **186**, 363-381.e19 (2023).

63. Renier, N. *et al.* iDISCO: A Simple, Rapid Method to Immunolabel Large Tissue Samples for Volume Imaging. *Cell* **159**, 896–910 (2014).

64. Tomer, R., Ye, L., Hsueh, B. & Deisseroth, K. Advanced CLARITY for rapid and high-resolution imaging of intact tissues. *Nat Protoc* **9**, 1682–1697 (2014).

65. Tanaka, N. *et al.* Whole-tissue biopsy phenotyping of three-dimensional tumours reveals patterns of cancer heterogeneity. *Nat Biomed Eng* **1**, 796–806 (2017).

66. Murray, E. *et al.* Simple, Scalable Proteomic Imaging for High-Dimensional Profiling of Intact Systems. *Cell* **163**, 1500–1514 (2015).

67. Chen, B.-C. *et al.* Lattice light-sheet microscopy: Imaging molecules to embryos at high spatiotemporal resolution. *Science* **346**, 1257998 (2014).

68. Dean, K. M., Roudot, P., Welf, E. S., Danuser, G. & Fiolka, R. Deconvolution-free Subcellular Imaging with Axially Swept Light Sheet Microscopy. *Biophysical Journal* **108**, 2807–2815 (2015).

69. Scholaert, M. *et al. 3-D deconvolution of human skin immune architecture with Multiplex Annotated Tissue Imaging System (MANTIS)*. http://biorxiv.org/lookup/doi/10.1101/2023.01.13.523748 (2023) doi:10.1101/2023.01.13.523748.

70. Van Ineveld, R. L. *et al.* Revealing the spatio-phenotypic patterning of cells in healthy and tumor tissues with mLSR-3D and STAPL-3D. *Nat Biotechnol* **39**, 1239–1245 (2021).

71. Shi, L., Wei, M. & Min, W. Highly-Multiplexed Tissue Imaging with Raman Dyes. *JoVE* 63547 (2022) doi:10.3791/63547.

72. Stringer, C., Wang, T., Michaelos, M. & Pachitariu, M. Cellpose: a generalist algorithm for cellular segmentation. *Nat Methods* **18**, 100–106 (2021).

73. Zhou, D., Bousquet, O., Lal, T., Weston, J. & Schölkopf, B. Learning with Local and Global Consistency. in *Advances in Neural Information Processing Systems* (eds. Thrun, S., Saul, L. & Schölkopf, B.) vol. 16 (MIT Press, 2003).